Temperature evolution of the Gd magnetization profile in strongly coupled Gd/Fe multilayers

Y. Choi,[1,2] D. Haskel,[2] R. E. Camley,[3] D. R. Lee,[2] J. C. Lang,[2] G. Srajer,[2] J. S. Jiang,[4] and S. D. Bader[4]
[1]*Department of Materials Science and Engineering, Northwestern University, Evanston, Illinois 60208, USA*
[2]*Advanced Photon Source, Argonne National Laboratory, Argonne, Illinois 60439, USA*
[3]*Department of Physics, University of Colorado, Colorado Springs, Colorado 80907, USA*
[4]*Materials Science Division, Argonne National Laboratory, Argonne, Illinois 60439, USA*
(Received 20 January 2004; revised manuscript received 18 May 2004; published 27 October 2004)

The temperature evolution of the magnetization depth profile in Gd layers of a strongly coupled $[\mathrm{Gd}(50\ \text{Å})/\mathrm{Fe}(15\ \text{Å})]_{15}$ multilayer is studied using x-ray resonant magnetic scattering (XRMS) and x-ray magnetic circular dichroism (XMCD) techniques. XRMS yields a spatially resolved, element-specific, magnetization depth profile, while XMCD spatially averages over this profile. The combined data inequivocally show the presence of an inhomogeneous magnetic profile within the Gd layers at all measured temperatures between 20 and 300 K. These inhomogeneous profiles, which feature enhanced magnetic ordering near the Gd/Fe interface, were refined using both a kinematic Born approximation and a recently developed distorted-wave Born approximation, both of which include the contribution of structural and magnetic interfacial roughness. Calculations of the static magnetic configuration within a mean-field approach that neglects interfacial roughness are in agreement with the measured inhomogeneous profile and its temperature evolution. The results suggest that the enhanced Gd magnetization near the interface arises from its proximity to magnetically ordered Fe.

DOI: 10.1103/PhysRevB.70.134420 PACS number(s): 75.70.−i, 75.25.+z, 75.75.+a

I. INTRODUCTION

Interfaces play a fundamental role in determining the properties of thin film magnetic devices. Examples include interfacial roughness effects on the giant magnetoresistance (GMR) of spin-valve structures,[1] spin transport across interfaces,[2] and exchange biasing[3] at the interface between an antiferromagnet and a ferromagnet which can yield enhancement of magnetic ordering temperature due to the proximity effect.[4] Interfaces and surfaces can also act as nucleation centers for inhomogeneous magnetization depth profiles[5–7] and be responsible for chirality in some magnetic structures.[8] Magnetic behavior at surfaces and interfaces often differs from the bulk behavior. For example, on Gd surface layers, enhanced magnetic ordering temperature and magnetization were observed.[9–11] On multilayers of Gd and nonmagnetic Y, a reduced Gd-magnetic moment near interfaces was also reported.[12,13] In Gd/Fe multilayers, the strong coupling between Gd and Fe at the interfaces causes Gd magnetization to persist above the Curie temperature of bulk Gd. This enhancement of Gd layer magnetization near the interfaces was observed by spin-polarized Auger-electron spectroscopy[14] and by x-ray resonant techniques.[15,16]

The origin of many of the above mentioned magnetic phenomena at surfaces and interfaces is not fully understood. While a proximity effect can possibly account for the observed enhancement or reduction of magnetization at interfaces, other sources need to be considered including the effect of intermixing and roughness. The experimental characterization of magnetic interfaces is difficult because of their small fractional volume and buried nature. X-ray and neutron techniques have been widely used to probe magnetic interfaces in thin films.[12,13,15–19,22–25] In particular, x rays have been very valuable for studies of magnetism through x-ray magnetic circular dichroism[26,27] (XMCD) and x-ray resonant magnetic scattering[28,29] (XRMS) techniques. The combination of XMCD with x-ray standing waves (XSW) has also been used in order to separate interfacial and bulk magnetization.[17] The advantage of x-ray-based techniques is in their elemental specificity, which permits the separation of magnetic contributions from different atomic species. Whether through the absorption process of XMCD or the resonant scattering process of XRMS, the excited photoelectron present in the final or intermediate state acquires a spin polarization through the spin-orbit coupling interaction. Thus, it becomes sensitive to the spin imbalance in the unoccupied density of states near the Fermi energy. By measuring the difference in absorption or scattering of x rays with opposite helicities, a measurement of this spin imbalance is obtained, which is proportional to the absorbing or scattering atom's net magnetic moment.

An enhanced magnetization in the Gd layer near Gd/Fe interfaces of a $[\mathrm{Gd}(54\ \text{Å})/\mathrm{Fe}(35\ \text{Å})]_{15}$ multilayer was observed by Ishimatsu *et al.*, [16] using XRMS and Mössbauer spectroscopy. Their XRMS measurements near the compensation point (where Gd and Fe magnetizations are equal but opposite yielding zero net magnetization[30]) revealed a twisting of the Gd magnetization with respect to the applied field direction. To analyze their XRMS data, a dynamical calculation was used but structural and magnetic roughness were neglected. Similarly, for the analysis of XRMS data from Ce/Fe multilayers, Jaouen and co-workers[19] assumed a perfect multilayer in deriving the magnetization profile in α-Ce layers and noted that their fitted magnetization amplitude was overestimated. Since phase information is lost in a measurement of XRMS intensity, the XRMS data cannot be inverted to directly yield the magnetization depth profile. It has to be deduced by fitting theoretical models to the data. Accurate determination of magnetization requires proper

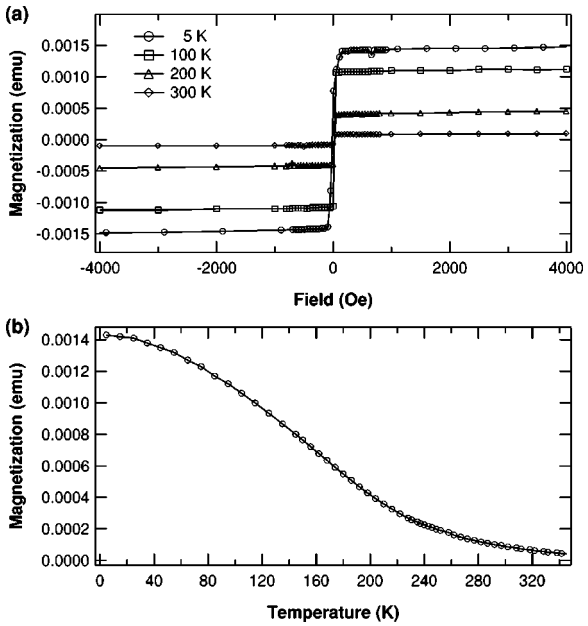

FIG. 1. SQUID magnetometry measurements on the Gd/Fe multilayer. (a) Magnetization as a function of field at temperatures 20, 100, 200, and 300 K. (b) Magnetization as a function of temperature under 1000 Oe field.

treatment of chemical and magnetic roughnesses since both affect the amplitude of the XRMS signal.[20,21]

In a previous study of $[\mathrm{Gd}(50\ \text{Å})/\mathrm{Fe}(15\ \text{Å})]_{15}$ magnetic multilayers,[15] we focused on the enhanced magnetic coupling near Gd/Fe interfaces. A Born approximation (BA), modified to include roughness, absorption, and refraction, was used to interpret the XRMS data. This kinematic, single scattering, approximation is only valid away from the regime of total external reflection. Here, we extend this study by using the distorted-wave Born approximation[21,31] (DWBA), which includes multiple scattering and roughness to derive the temperature evolution of the Gd magnetization profile and to further explore the origin of enhanced interfacial Gd magnetization. To that effect, mean-field theoretical calculations of the static spin configurations at different temperatures were conducted and compared with the experiment.

In Sec. II of this paper, we describe the XMCD and XRMS experiments on a Gd/Fe multilayer. In Sec. III, the XRMS data are fitted with theoretical expressions derived from the DWBA, and the results are compared with those using the BA. Section IV presents temperature-dependent Gd layer magnetization profiles derived from the XMCD and XRMS experiments and their comparison with theoretical calculations within a mean-field approach. Section V summarizes the results.

II. EXPERIMENTS AND RESULTS

The multilayer used in this study was sputtered in vacuum onto a Si substrate with Nb buffer (100 Å) and cap (30 Å) layers. The multilayer **(**$[\mathrm{Gd}(50\ \text{Å})/\mathrm{Fe}(15\ \text{Å})]_{15}$**)** has 15 bilayers and an extra Gd layer at the top, i.e., Gd termination at both ends. SQUID measurements in Fig. 1 reveal that up to 350 K the multilayer is in the Gd-aligned phase at moderate fields,[30] where the Gd magnetization is parallel to the applied field direction and the Fe magnetization is antiparallel. Up to 350 K, Fig. 1(b) does not show a compensation point above which the moment would increase again.

X-ray measurements were performed at the 4-ID-D beamline of the Advanced Photon Source at Argonne National Laboratory. Undulator radiation was passed through double Si monochromators, and a diamond (111) quarter-wave plate operated in Bragg transmission geometry was used to produce the circularly polarized x rays.[32] The 2.1 kOe field of a permanent magnet was applied parallel to the sample surface and in the scattering plane in order to align the Gd moment parallel to the applied field at all temperatures considered. The sample and the magnet were placed inside a closed-cycle He refrigerator mounted on a diffractometer.

The XRMS measurements were performed in reflectivity mode. The incident photon energy was tuned to near the Gd L_2 absorption edge (7929 eV), and the reflected intensities were measured as a function of the incident angle while flipping the helicity of the circularly polarized incident x rays. For the reflectivity measurements, I^+ and I^- refer to the reflected intensities for opposite helicities. The XMCD measurements were performed in fluorescence mode by monitoring the intensity of Gd $L\beta$ radiation while alternating the helicity at each energy through the Gd L_2 edge. For the XMCD measurements, I^+ and I^- refer to $L\beta$ fluorescence intensities for the two opposite helicities. The incident angle was 10°, for which the x-ray penetration depth is much larger than the multilayer thickness.

Resonant scattering factors of Gd atoms were obtained from absorption measurements through the L_2 absorption edge. The absorption, $\mu_e=[(\mu^+ + \mu^-)/2]$, and dichroism, $\mu_m = [\mu^+ - \mu^-]$, spectra were measured by alternating between opposite helicities of incoming x rays at each photon energy with fixed applied magnetic field.

The imaginary parts of chemical and magnetic resonant scattering factors, $f''_{e,m}$, are related to the measured absorption spectra of Gd through the optical theorem, $f''_{e,m} \propto \mu_{e,m}$, and the real parts, $f'_{e,m}$, were obtained using differential Kramers–Kronig transforms. The procedure uses tabulated scattering factors away from resonance for absolute normalization.[33,34] Resonant scattering factors for Gd are shown in Fig. 2. Since the real part of the magnetic scattering factor dominates the resonant magnetic scattering, the incident photon energy was tuned to 7929 eV, where f'_m is maximized.

To eliminate any experimental artifacts in our dichroic signals, absorption and scattering measurements were taken with applied fields parallel and antiparallel to the photon wave vector. At each temperature, two measurements were performed at $\phi = 0°$ and 180° where ϕ is defined as the angle between the incoming x-ray beam and the applied field. Figure 3 shows absorption measurements across the Gd L_2 absorption edge. The dichroic process leads to complete sign reversal for opposite orientations of $\hat{k}_i$ and $\hat{H}$. Incomplete reversal is due to systematic errors. These errors were only a few percent in our measurements and were subtracted from the data before integrating the XMCD signal to obtain average magnetization in Gd layers.

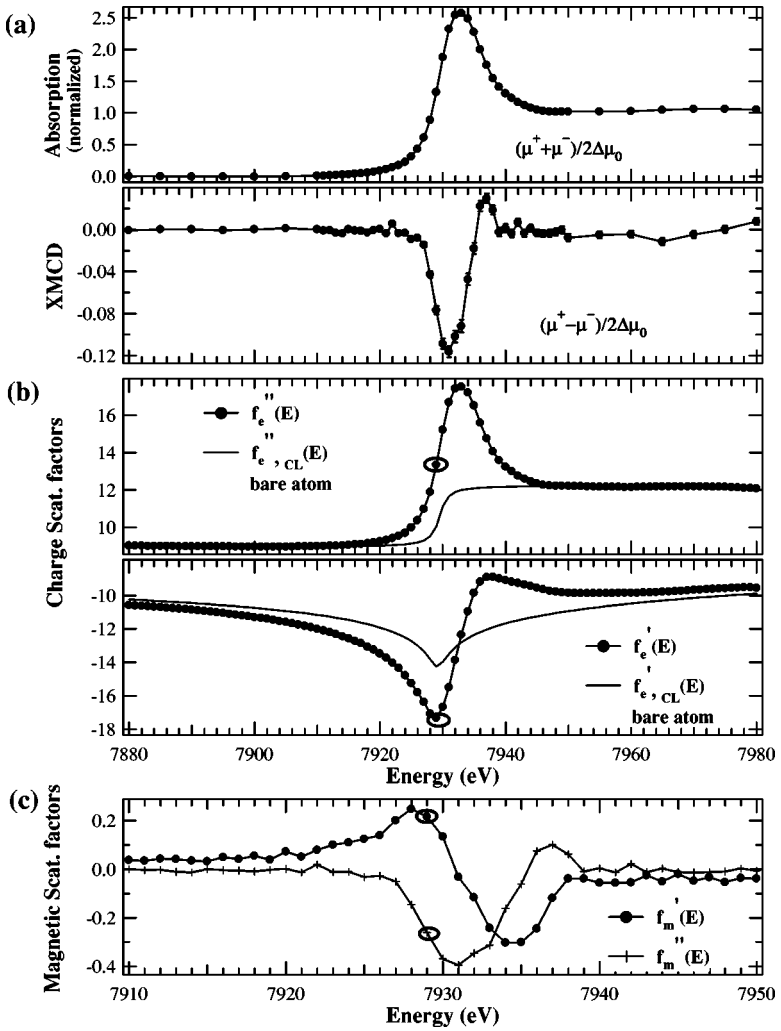

FIG. 2. Absorption measurements in fluorescence geometry near the Gd L_2 edge at $T=20$ K, and 2.1 kOe applied field. (a) Edge-jump normalized sum and difference of the two intensities with opposite helicities. Charge (b) and magnetic (c) scattering factors across the Gd L_2 edge. (b) shows tabulated atomic scattering factors for a single atom ($f'^{(n)}_{e,CL}$) and experimentally derived atomic scattering factors including solid-state effects ($f'^{(n)}_{e}$). The circles on the graphs denote the energy at which the reflectivity measurements were performed.

Figure 4 shows the XMCD signal at temperatures from 20 to 300 K. We used the integrated area under these peaks to estimate the relative magnetization of Gd layers at each temperature. The sign of XMCD signal does not change between 20 and 300 K, and this indicates that, at least up to 300 K, the Gd/Fe multilayer does not go through a compensation point above which the Gd XMCD signal would reverse its sign.

Figure 5 shows x-ray specular reflectivity curves from the $[\mathrm{Gd}(50\ \text{Å})/\mathrm{Fe}(15\ \text{Å})]_{15}$ multilayer with the incident photon energy at 7929 eV. The measurements were done at four different temperatures, 20, 100, 200, and 300 K. The charge specular reflectivity curve [Fig. 5(a)] was obtained by adding scattering intensities for opposite helicities ($I^+ + I^-$), and the magnetic sensitive reflectivity curves [Figs. 5(b)–5(e)] were obtained by taking the difference between the two intensities ($I^+ - I^-$). Changes in the charge specular reflectivity curves at different temperatures were negligible, indicating negligible structural change. However, in the difference signal, significant changes occur due to temperature-dependent changes in the magnetization depth profile of the Gd layers.

As mentioned earlier, SQUID measurements indicate that for the moderate field of $\mathbf{H}=2.1$ kOe the Gd/Fe multilayer is in the Gd-aligned state (Fig. 1). This implies that there is no magnetic component perpendicular to the applied field direction. Since the difference cross section measures the magnetic component in the scattering plane (see Sec. III), an aligned phase will result in zero difference signal if the field is applied perpendicular to this plane. This is shown in Fig. 6, where we rotated the sample and magnet assembly by 90° ($\phi=90°$), yielding a negligible difference between the scattered intensities for the two helicities.

III. MODELING OF XRMS DATA

Assuming negligible nonresonant magnetic scattering and using the electric dipole approximation, the resonant elastic scattering length for a Gd ion can be written as[29]

$$f = (f_0 + f_e)(\hat{\epsilon}'^* \cdot \hat{\epsilon}) + i f_m (\hat{\epsilon}'^* \times \hat{\epsilon}) \cdot \hat{m} + f_l (\hat{\epsilon}'^* \cdot \hat{m})(\hat{\epsilon} \cdot \hat{m}), \tag{1}$$

where $f_0 = -Zr_0$, f_e and f_m are anomalous charge and magnetic scattering lengths, $\hat{\epsilon}$, $\hat{\epsilon}'$ are polarization vectors of incoming, scattered radiation, $\hat{m}$ is local moment direction, and f_l is linear dichroic term. The last term is ignored since f_l is generally much smaller than f_m at lanthanide L edges and since the polarization vectors are nearly perpendicular to $\hat{m}$ for our scattering geometry. The scattering cross section obtained from Eq. (1) includes pure charge, pure magnetic, and charge-magnetic interference terms.[20]

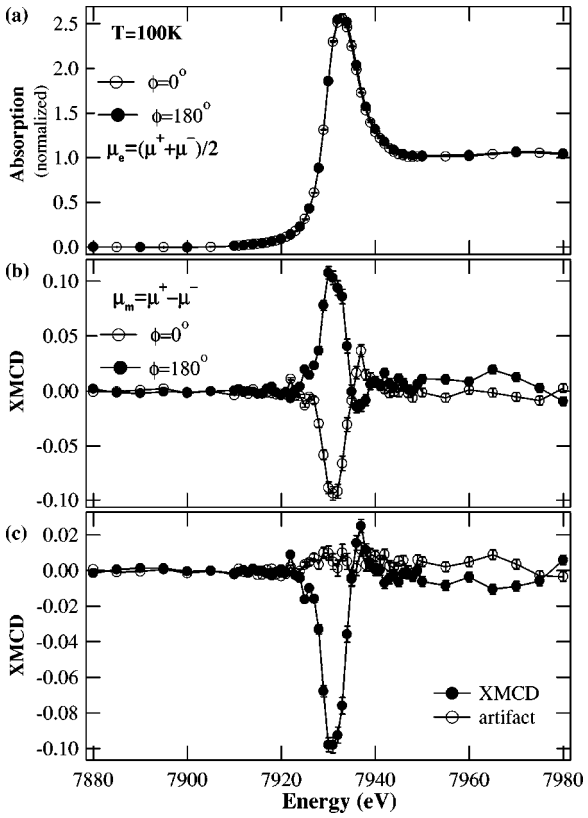

FIG. 3. The XMCD measurements for opposite orientations of photon wave vector and sample magnetization. The angle between the incoming beam and the applied field, 2.1 kOe, is ϕ. (a) Polarization-independent absorption coefficient obtained from the sum of fluorescence intensities for opposite helicities of the incoming radiation. (b) Difference in absorption coefficient for opposite x-ray helicities. (c) The XMCD signal is $[\mu_m(\phi=0°)-\mu_m(\phi=180°)]/2$, and nonmagnetic artifact is $[\mu_m(\phi=0°)+\mu_m(\phi=180°)]/2$.

Since only dipole transitions at L edges are considered, the magnetization profiles from charge-magnetic specular reflectivity fittings represent the profiles of Gd 5*d* moments. These are assumed to mimic the profiles of their 4*f* counterparts due to the strong (4*f*-5*d*) intra-atomic exchange coupling that contributes to the spin polarization of the Gd 5*d* band. This is supported by XMCD measurements on a series of $R_2Fe_{14}B$ intermetallics taken by Miguel-Soriano *et al.*[35]

To simplify the calculations, each Gd layer was divided into three sublayers. Equivalence of Gd/Fe and Fe/Gd interfaces was assumed so that the two outer sublayers near Fe have the same magnetization. Charge specular reflectivity curves were fitted with the DWBA,[21,31] which yields the same calculated reflectivity curves as the ones using Parratt's recursive formalism.[36] The fitted structural parameters from the charge specular reflectivity curves were then incorporated into the charge-magnetic specular reflectivity fittings using the DWBA.[21] For the different temperatures, each Gd layer (total 16 Gd layers) was divided into three sublayers. The middle sublayer thickness was a fitting parameter, while that of the equivalent outer sublayer was constrained by the total layer thickness fitted from the charge specular data.

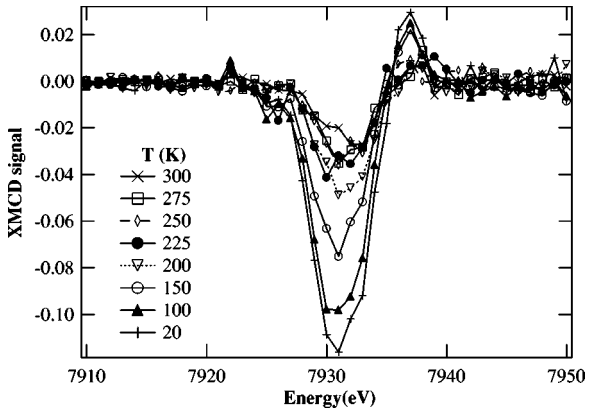

FIG. 4. Gd L_2 edge XMCD at temperatures between 20 and 300 K with 2.1 kOe applied field. The integrated areas under the curves were used to obtain relative magnetization of the Gd layers at each temperature.

Other fitting parameters are the magnetic roughness between the layers and the relative magnetization in the three Gd sublayers. These charge and magnetic parameters were used to calculate the charge and charge-magnetic reflectivity curves using the BA.

The edge-jump normalized (i.e., per atom) Gd XMCD peak signal at 10 K is $\mu_m/\mu_e=0.051(3)$, in agreement with bulk Gd. In addition to full saturation, this indicates that the Gd magnetic moment is not reduced relative to its bulk value. The experimentally determined value of f_m at 10 K therefore sets the scale for quantitative determination of depth resolved magnetization profiles on an absolute scale. A scaling of f_m was used in modeling the local Gd magnetization at each temperature.

A. First Born approximation model for calculation of charge-magnetic specular reflectivity

Charge-magnetic specular reflectivity curves calculated using the BA are shown as gray lines in Fig. 5. These curves were calculated using the BA with the fitted DWBA parameters (Sec. III B).

Using the BA, the differential cross section is written

$$\frac{d\sigma}{d\Omega}=\left[n_e(f_0+f_e)\hat{\epsilon}'^{*}\cdot\hat{\epsilon}\int\int\int_{V_{charge}}e^{i\hat{q}\cdot\hat{r}}d^3r + in_e f_m(\hat{\epsilon}'^{*}\hat{\epsilon})\cdot\hat{m}\int\int\int_{V_{mag}}e^{i\hat{q}\cdot\hat{r}}d^3r\right]^2, \quad (2)$$

where n_e is the scatterer's number density, and the integrals are over the charge and magnetic volume. After squaring the sum of the charge and magnetic terms, the cross section has a pure charge term, a pure magnetic term, and a charge-magnetic interference term. Only the latter depends on the orientation of magnetization (or helicity). Therefore, the difference in the scattering intensities between the two opposite helicities, I^+-I^-, is due to the charge-magnetic interference contribution only. The charge-magnetic interference term of the scattering cross section includes the products of the

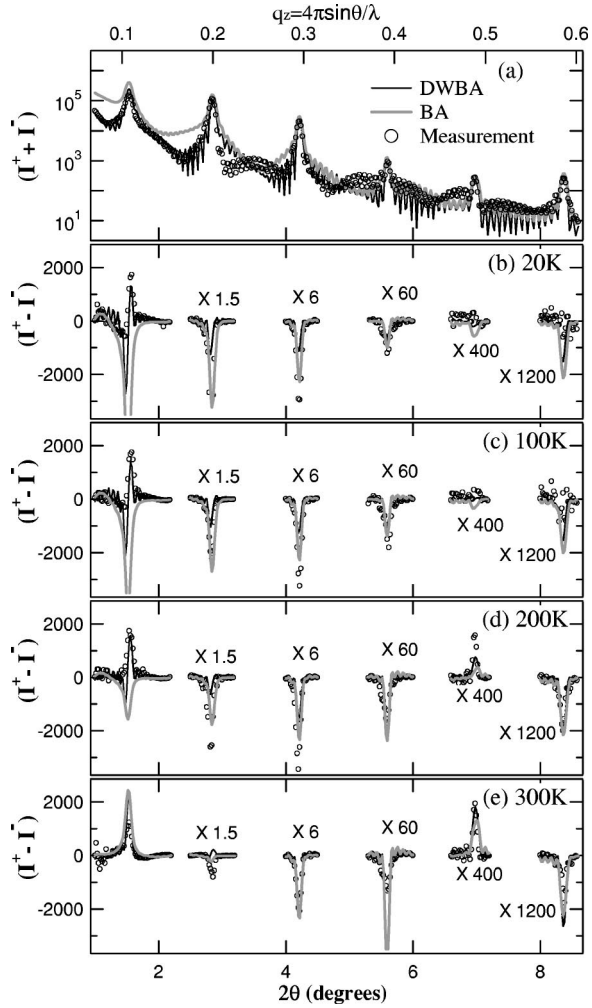

FIG. 5. Specular reflectivity measurements (symbols), the DWBA calculation (dark lines), the BA calculation (gray lines). The measurements were performed with an incoming photon energy of 7929 eV and 2.1 kOe applied field. The measured reflectivity curves were fitted with the DWBA theory, and the parameters obtained from this fitting were used for the BA calculation. (a) Charge specular reflectivity for Gd/Fe multilayer at 300 K. The root-mean-squared roughness of the Gd/Fe chemical interface was 3.0 ± 1.1 Å, and the densities of Gd and Fe layers were 93% of their bulk values. (b)–(e) Charge-magnetic reflectivity curves at the indicated temperatures with fits using the BA and DWBA theories.

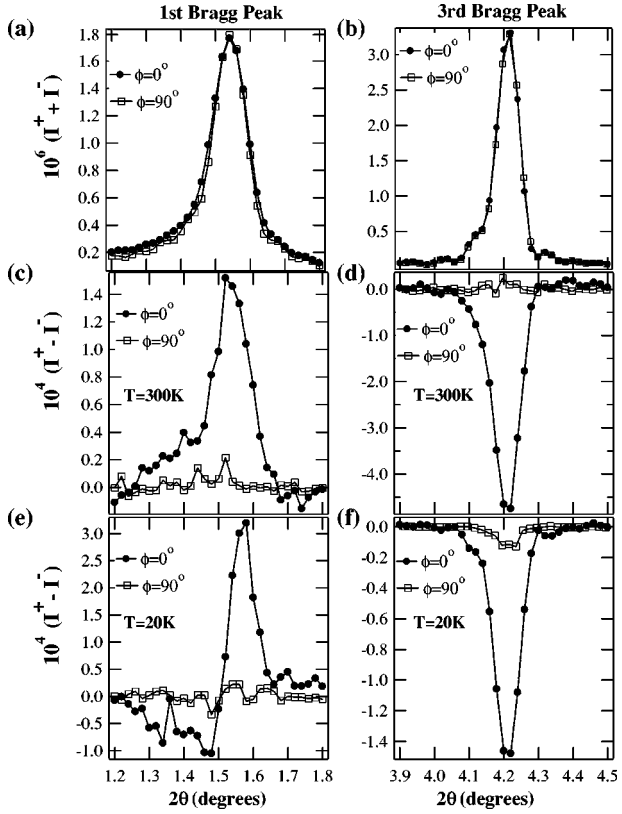

FIG. 6. The XRMS measurements at $\phi = 0°$ and 90° where ϕ is the angle between the applied field and the beam direction. (a) and (b) are charge peaks, and (c)–(f) are charge-magnetic peaks for the first and third multilayer Bragg peak. (c)–(f) show that there is no magnetization component perpendicular to the applied field direction.

charge and magnetic contrasts at the interfaces. Adding charge and magnetic roughnesses at the interfaces, the charge-magnetic cross section for specular reflectivity becomes[15,20,31,37]

$$\left(\frac{d\sigma}{d\Omega}\right)_{charge\text{-}mag} = \frac{4\pi^2 L_x L_y \delta(q_x)\delta(q_y)}{q_z^2} \times P_c[\cos 2\theta(\hat{k}_i \cdot \hat{m}) + (\hat{k}_f \cdot \hat{m})] \sum_{i,j}^{N} e^{iq_z(z_i - z_j)} \times [\Delta\rho_{e,i}^* \Delta\rho_{m,j} e^{-(q_z^2/2)(\sigma_{e,i}^2 + \sigma_{m,j}^2)} + \Delta\rho_{e,j} \Delta\rho_{m,i}^* e^{-(q_z^2/2)(\sigma_{e,j}^2 + \sigma_{m,i}^2)}],$$

$$\Delta\rho_{e,i}^* = n_e^{i+1}(f_0 + f_e^*)^{i+1} - n_e^i (f_0 + f_e^*)^i,$$

$$\Delta\rho_{m,j} = n_e^{j+1} s_m^{j+1} f_m^{j+1} - n_e^j s_m^j f_m^j. \quad (3)$$

Here, q_z, θ_{eff}, δ_{eff}, and β_{eff} are defined as

$$q_z = \frac{4\pi \sin \theta_{eff}}{\lambda},$$

$$\theta_{eff} = \sqrt{\theta^2 - 2\delta_{eff} - i2\beta_{eff}},$$

$$\delta, \beta_{eff} = \frac{d_{\mathrm{Fe}}}{d_{\mathrm{Fe}} + d_{\mathrm{Gd}}} \delta, \beta_{\mathrm{Fe}} + \frac{d_{\mathrm{Gd}}}{d_{\mathrm{Fe}} + d_{\mathrm{Gd}}} \delta, \beta_{\mathrm{Gd}}. \quad (4)$$

The charge and magnetic density contrasts across interfaces i, j are $\Delta\rho_{e,i}^*$ and $\Delta\rho_{m,j}$, respectively. The degree of circular polarization is P_c; n_e is the atomic number density; s_m is a scaling factor for the magnetization; $\hat{k}_{i,f}$ are wave vectors of the incident and scattered radiation. Height fluctuations about the average positions of the charge and magnetic interfaces are assumed to be Gaussian, and thus $\langle[\delta z_{e,m}(x,y)]^2\rangle = \sigma_{e,m}^2$. Orientational disorder contributions to the magnetic roughness are not explicitly considered, i.e., they are folded into an *effective* magnetic roughness σ_m.

The polarization dependence in Eq. (3) was calculated using the matrix formalism of Blume and Gibbs[38] for the case where no polarization analysis of the scattered beam is performed. It involves taking traces over matrix products of the form $\langle \hat{\epsilon}'^{*} \cdot \hat{\epsilon} \rangle \rho \langle [(\hat{\epsilon}'^{*} \times \hat{\epsilon}) \cdot \hat{m}]^{*} \rangle$, where ρ is the (2×2) density matrix of a beam with circular polarization in the (σ, π) basis. From Eq. (3), the charge-magnetic cross section is only sensitive to the component of the magnetization density in the scattering plane $[(\hat{k}_i \cdot \hat{m}), (\hat{k}_f \cdot \hat{m})$ terms].

B. Distorted-wave Born approximation model for fitting of charge-magnetic specular reflectivity

In Fig. 5, fitted curves using the DWBA are shown as dark solid lines. The DWBA calculations for the charge-magnetic reflectivity are based on a recursive formalism originally developed by Stepanov and Sinha[39] for resonant specular reflectivity from magnetic multilayers with smooth interfaces, and recently extended by Lee *et al.* to include interfacial roughness.[21] In this formalism, the Nevot-Croce formula for specular reflectivity[36] was generalized for the case of a single, rough, magnetic interface using a self-consistent method and then extended to multiple interfaces.

For the specular condition, the differential cross section for scattering by a rough surface can be written as[21,31]

$$\frac{d\sigma}{d\Omega} = \frac{1}{16\pi^2} |\langle T^{fi} \rangle|^2. \tag{5}$$

Here, $T^{fi} = \langle \hat{k}_f, \nu | T | \hat{k}_i, \mu \rangle$ is the scattering matrix element. Wave vectors of incident and scattered radiation are $k_{i,f}$, and μ and ν are polarization vectors. The scattering matrix element is expressed as

$$\begin{aligned} \langle k_f, \nu | T | k_i, \mu \rangle = {} & k_0^2 \langle -k_f^t, \nu | \chi^{(0)} | E_\mu^i(r) \rangle + k_0^2 \langle -k_f^t, \nu | \Delta^e | k_i, \mu \rangle \\ & + k_0^2 \langle -k_f^t, \nu | \Delta^m | k_i, \mu \rangle, \end{aligned} \tag{6}$$

where $E_\mu^i(r)$ is the incident wave and $|-k_f^t, \nu\rangle$ is the time-reversed function corresponding to a wave incident on the interface. An ideal system with a smooth interface is denoted by $\chi^{(0)}$, and Δ^e and Δ^m are structural and magnetic perturbations on $\chi^{(0)}$ due to roughness.

For the specular condition, Eq. (6) can be rewritten as

$$\mathbf{R}_{\nu\mu} = \mathbf{R}_{\nu\mu}^{(0)} + \mathbf{U}_{\nu\mu} + \sum_{\lambda} \mathbf{V}_{\nu\lambda} \mathbf{R}_{\lambda\mu}^{(0)}, \tag{7}$$

where $R_{\nu\mu}, R_{\nu\mu}^{(0)}$ are reflection coefficients for rough and smooth ideal interfaces, respectively. The term $R_{\nu\mu}^{(0)}$ can be expressed in terms of 2×2 matrices using the polarization bases for the incident and reflected waves. For the waves in the nonmagnetic medium, the polarization base is given by $(\hat{\epsilon}_\sigma, \hat{\epsilon}_\pi)$. In the magnetic resonant medium, the polarization base is expressed by two circular polarizations, $(\hat{\epsilon}^{(1)}, \hat{\epsilon}^{(2)})$, where $\hat{\epsilon}^{(1)} = \hat{\epsilon}_\sigma + i\hat{\epsilon}_\pi$ and $\hat{\epsilon}^{(1)} = \hat{\epsilon}_\sigma - i\hat{\epsilon}_\pi$. In the above equation, $U_{\nu\mu}, V_{\nu\lambda}$ are the correlation terms due to the roughness in the reflection coefficients containing structural and magnetic roughness (σ_e and σ_m). A self-consistent matrix can be written as

TABLE I. Parameters derived from fits to the charge-magnetic specular reflectivity data for the indicated temperatures. The relative magnetization of the Gd sublayers are M_{int} and M_{mid}. For all temperatures, $\sigma_{e,\text{GdFe}} = 3.0 \pm 1.1$ Å, $\sigma_{e,\text{GdGd}} = 0$ Å. The fitted thickness of Gd sublayers adjacent to the Fe layers is $d_{\text{int}} = 3.94 \pm 0.09$ Å at all temperatures.

T (K)	M_{int}	M_{mid}	$\sigma_{m,\text{GdFe}}$ (Å)	$\sigma_{m,\text{GdGd}}$ (Å)
300	1.00±0.12	0.00±0.00	4.21±0.23	3.18±0.06
200	1.00±0.13	0.46±0.04	3.89±0.14	3.26±0.13
100	1.00±0.13	0.74±0.04	3.76±0.09	3.61±0.23
20	1.00±0.13	0.91±0.03	3.66±0.06	3.44±0.31

$$\mathbf{R} = \mathbf{R}^{(0)} + \mathbf{U} + \mathbf{V}\mathbf{R}, \tag{8}$$

where its solution is

$$\mathbf{R} = (1 - \mathbf{V})^{-1} (\mathbf{R}^{(0)} + \mathbf{U}). \tag{9}$$

Reflection coefficients are expressed as three different functions for nonmagnetic/magnetic (nonresonant/resonant), magnetic/nonmagnetic (resonant/nonresonant), and magnetic/magnetic interfaces (resonant/resonant). These reflectivity coefficients can be expressed as a function of the refracted angles $u_\pm$, the wave vector k_o, the roughness $\sigma_{e,m}$, and the dielectric susceptibility. These functions are described in detail elsewhere.[21]

IV. ANALYSIS AND DISCUSSION

The parameters obtained by fitting the measured reflectivity curves with the DWBA model are shown in Table I. The fitted charge-magnetic specular curves simulated with these parameters are shown as dark solid lines in Figs. 5(b)–5(e). It is assumed that there is no charge roughness between the Gd sublayers ($\sigma_{e,\text{GdGd}} = 0$).

With these parameters, the charge-magnetic specular reflectivity curves were calculated using the BA model [Figs. 5(b)–5(e), gray solid lines]. Overall, both models are in agreement with the data except near the first multilayer Bragg peak. In the low q_z region near the critical angle for total external reflection, the BA model does not explain the charge-magnetic specular reflectivity because it neglects multiple scattering and only approximates the x-ray refraction, both of which are strong near total external reflection. The DWBA is a dynamical calculation taking account of the multiple scattering and thus gives a better description in this region, as also found in nonmagnetic cases.[31] Since both the BA and the DWBA models give consistent magnetic parameters in the fits, however, the BA model can be used provided a large q_z range of data are available. An extended q_z range is a prerequisite for refinements of magnetization density profiles with high spatial resolution. Furthermore, since the BA model is a kinematical calculation wherein each interface acts as an independent scatterer, it is conceptually more straightforward than the DWBA model, which needs a recursive approach to treat multiple interfaces.

As shown in Table I, the Gd moment of the interfacial regions are enhanced relative to that of the interior regions.

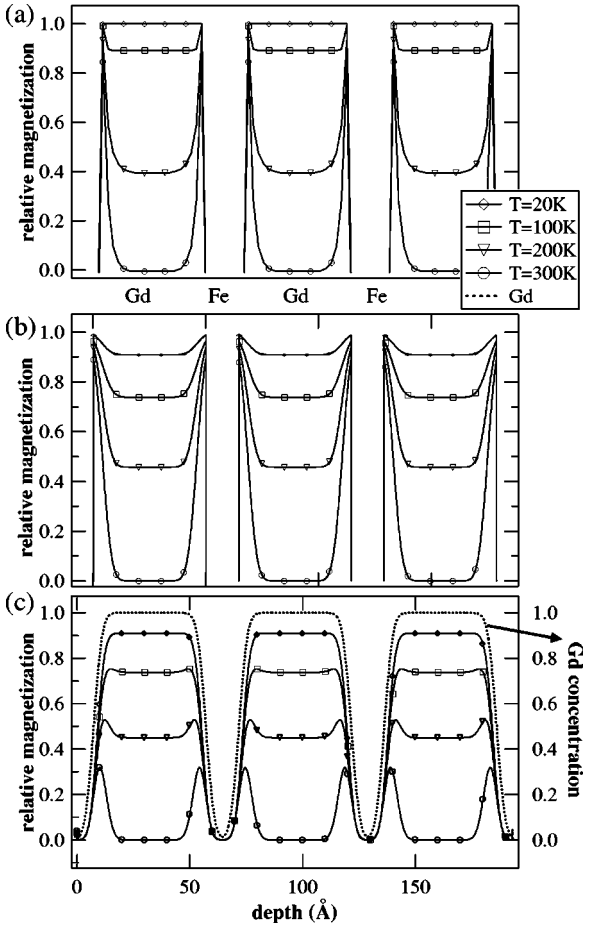

FIG. 7. (a) Gd magnetization profile obtained by mean-field calculations, assuming perfect interfaces. (b) Gd magnetization profile used in fitting the charge-magnetic reflectivity data at the different temperatures. For comparison with (a), charge and magnetic roughnesses between Gd/Fe layers are not included in this plot. (c) As in (b), but with structural and magnetic roughness included. The dashed line represents Gd concentration obtained from charge reflectivity fitting. Each profile shows the relative magnetization within the Gd layer, which is the product of Gd concentration and the average magnetic moment within each Gd sublayer (Ref. 12).

While the Gd moment of interior regions decreases as the temperature increases, the enhanced moment in the interfacial regions does not change. The width of these magnetized regions is 3.94 ± 0.09 Å, almost independent of temperature. The fitted magnetic roughnesses ($\sigma_{m,\mathrm{GdFe}}, \sigma_{m,\mathrm{GdGd}}$) do not change noticeably as the temperature changes. However, it can be noted that the magnetic roughness between Fe and Gd layers ($\sigma_{m,\mathrm{GdFe}}$) slightly increases as the temperature increases.

The theoretical Gd magnetization profile at each temperature was calculated for the sample structure within a mean-field approach considering nearest-neighbor interactions only.[30] The results of these mean-field calculations at each temperature are shown in Fig. 7 along with the profiles derived from fits to the charge-magnetic specular reflectivity curves. The key parameters used in the mean-field calculation are: applied field =2.1 kOe; 20 Gd atomic layers per unit cell; 8 Fe atomic layers per unit cell; 15 unit cells with Gd on the outside at both ends; Gd moment $=7.0\ \mu_B$; Fe moment $=2.2\ \mu_B$. An initial estimate of the exchange-coupling parameters is made from the bulk Curie temperatures of Fe and Gd, where $T_C = J_{\mathrm{tot}} S(S+1)/3$. The exchange constant J_{tot} is expressed in Kelvins and is a measure of the total effective exchange field acting on an individual spin; it includes in-plane contributions as well as exchange fields from one plane acting on a neighboring plane. In the final calculations, the values for the exchange constants are $J_{\mathrm{Gd/Fe}} = -200$ K, $J_{\mathrm{Gd}} = 13.7$ K, and $J_{\mathrm{Fe}} = 529.3$ K. We expect that the exchange coupling within a plane will be the same as that between planes, so $J_{\mathrm{tot\text{-}Fe}} = 3\ J_{\mathrm{Fe}}$, for example. To obtain the best agreement with the data, a reduction factor of 0.9 was introduced for the Gd moments, and a reduction factor of 0.93 was included for the Fe moments. Additional details on the calculation and the choices of parameters can be found in Ref. 25.

As shown in Fig. 7 the profiles obtained from the mean-field calculation and those from the fitted parameters are consistent. Both theoretical and experimental results show that the Gd layers near Fe are fully magnetized at all temperatures considered while the magnetization in the interior decreases with increasing temperature.

One possible origin of the enhanced Gd magnetization (as observed in the experiments and in the mean-field calculations) is proximity to magnetized Fe ($T_c = 1024$ K) to which the Gd magnetization couples by a strong antiferromagnetic exchange interaction. This interlayer exchange interaction is short ranged, and therefore the enhancement in the Gd magnetization is limited to the region near the Gd/Fe interfaces. This scenario is supported by the results of mean-field calculations, which yield very similar magnetization profiles by assuming strong interlayer antiferromagnetic coupling across sharp interfaces. It is known that, in rare-earth (RE) transition-metal (TM) intermetallics, a strong coupling between TM and RE ions exists through strong hybridization between the RE 5*d* and TM 3*d* bands. Since Fe has a much higher ordering temperature than Gd, it induces spin polarization in the Gd 5*d* band through hybridization. The Gd 5*d* bands play a role in mediating the indirect coupling between localized Gd 4*f* moments.[40,41]

It can also be argued that the enhancement in the Gd magnetization near Gd/Fe interfaces is due to alloying between Gd and Fe. To address this question, off-specular, longitudinal, diffuse scattering measurements were performed on the same Gd/Fe sample. The data in Fig. 8(a) show Bragg peaks corresponding to the Gd/Fe bilayer period, indicating that the roughnesses at the Gd/Fe interfaces are conformal, i.e., correlated in the normal direction.[42] This indicates the presence of well-defined interfaces with pure roughnesses [Fig. 8(b)] as opposed to the structureless interfaces expected from pure intermixing [Fig. 8(c)]. The question remains whether structural roughness is needed to drive the interface magnetic ordering of Gd. Our theoretical calculations, which yield similar enhancements by assuming sharp interfaces, indicate that the strong antiferromagnetic coupling is the key ingredient. However, the spatial extent of the magnetized region is likely to be determined by a combination of structural roughness and the range of antiferromagnetic interac-

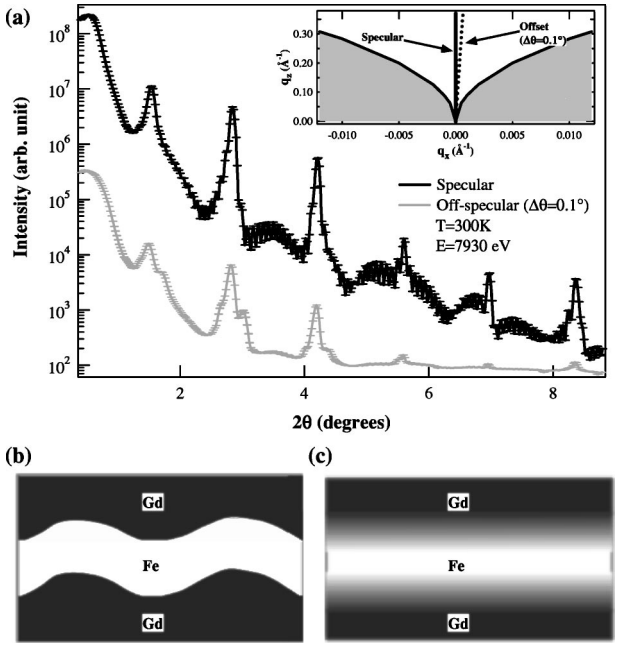

FIG. 8. (a) Specular reflectivity (dark) and off-specular reflectivity (gray) measurements. The offset angle is 0.1° for the off-specular measurement. The inset shows the wave-vector transfer in the reciprocal plane. (b) Interface with roughness. (c) Interface with intermixing.

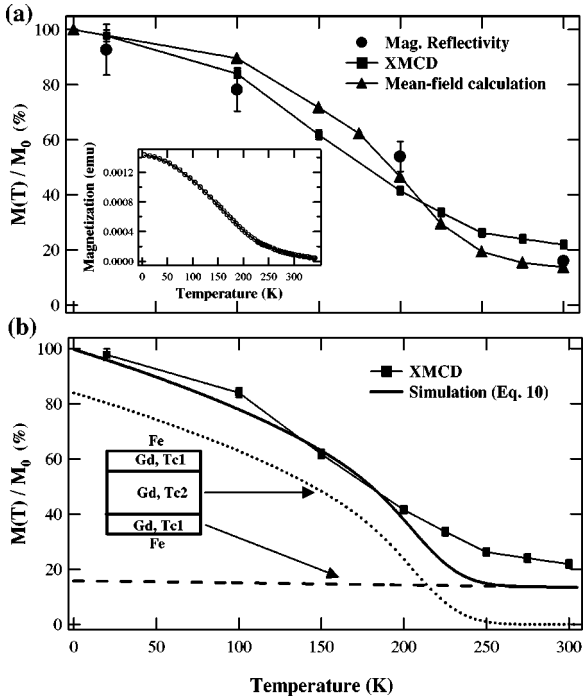

FIG. 9. Average Gd layer magnetization at each temperature. (a) XMCD result (rectangles) is obtained from temperature-dependent XMCD measurements by integrating the area under Gd L_2 absorption edge (Fig. 4). Mean-field calculation result (triangles) and charge-magnetic reflectivity result (circles) are calculated by integrating the area under Gd magnetization profile curves [Figs. 7(a) and 7(b), respectively]. The inset shows SQUID magnetometry result on the Gd/Fe multilayer (Fig. 1). (b) Magnetization for the interfacial (dashed line) and middle (dotted line) regions were calculated using Eq. (10) with different T_C values. The two values were added with the thickness ratio included (solid line).

tion between Gd and Fe. In this particular case, since the rms roughness is comparable to the extent of the magnetized Gd layer, the roughness sets an upper limit for the extent of such antiferromagnetic coupling.

Further evidence for the absence of significant intermixing comes from the XMCD measurements. We do not observe significant changes in XMCD line shape between 20 and 300 K, despite the latter probing the enhanced interfacial region only. Significant changes in local chemical environment associated with strong intermixing would have resulted in an altered line shape, which is not observed.

It is well known that the branching ratio between XMCD spectra taken over a pair of spin-orbit split edges (e.g., L_2 and L_3) can be related to the size of the orbital moment in the probed final state (e.g., 3*d* or 5*d*). In some cases, quantitative values of the size of the orbital moment can be obtained by applying sum rules to the integrals of the XMCD spectra.[43,44] At rare-earth *L* edges, however, these sum rules cannot be reliably applied to the measured spectra due to the strong exchange between the 4*f* and 5*d* bands.[45–47] This exchange not only spin polarizes the 5*d* band but produces a radial splitting within it, resulting in an asymmetry in the transition probability between the spin up and spin down electrons in the radial portion of the matrix elements. This spin dependence in the radial matrix elements is not included in the derivation of the sum rules and therefore quantitative measurements of the size of the rare-earth 5*d* moments are not possible. Nevertheless the branching ratio can still be used to obtain qualitative information about relative changes in the magnitude of the moments. Enhancements in the size of the orbital moment have been observed for thin magnetic films.[48] Similar changes might be expected in the Gd XMCD spectra taken at 20 K and 300 K since the spectra at 300 K probes only interfacial regions, while the spectra at 20 K probes the entire layer. We observed, however, no significant change in the total integral of the XMCD spectra across both edges, which was nearly zero at both temperatures. Thus the orbital moment for the Gd 5*d* states is negligible in both the central and interfacial regions.

The integrated area under the fitted magnetization profile (from the fitted parameters in Table I) is calculated to obtain the average magnetization of Gd layers for each temperature. This can be compared with similar averages obtained from the result of the mean-field calculations and with those obtained by integrating the XMCD data in Fig. 4. The figure shows that the mean-field calculation and the integrated moment calculation from the reflectivity fittings are in agreement. Assuming that each Gd layer has interfacial and interior regions with the same saturation magnetization M_0 but different T_C values, the average magnetization from the XMCD data was fitted using a superposition of two different $M(T)$ curves corresponding to interior and near-interface Gd volumes. The following equation was used to describe the temperature-dependent magnetization:[49]

$$\frac{M(T)}{M_0} = \int_{T_C} \left(\frac{T_C - T}{T_C} \right)^{\beta} \theta(T_C - T) \rho(T_C) dT_C, \qquad (10)$$

where $\theta(x)$ is the Heaviside function, and $\rho(T_C)$ is a Gaussian distribution function with a 20 K distribution width in order to account for disorder in the sputtered sample. The XMCD average magnetization result was reproduced best with $\beta = 0.47 \pm 0.09$. The contributions from the two regions were added as $M(T) = (2r)M_{\text{int}}(T) + (1-2r)M_{\text{bulk}}(T)$, where r is the ratio of interfacial region thickness over total Gd layer thickness ($r = 0.079$) obtained from XRMS measurements. The T_C value of the middle region is estimated to be 220 K, which is lower than that for bulk Gd ($T_c \approx 293$ K), consistent with other reports.[16] The T_C value of the interfacial regions is estimated to be 1050 K, which is comparable to the T_C value of bulk Fe. It should be noted that the moment of the interfacial regions is almost independent of temperature between 20 and 300 K, and this is consistent with the results from the reflectivity fitting (Table I). The large $J_{\text{Gd/Fe}}$ compared to J_{Gd} effectively decouples the Gd interfacial and bulk regions giving justification to the two-component system modeling in Fig. 9. Further support for this uncoupled behavior is found in the work of Binder and Hohenberg,[50] where decoupling of surface and bulk magnetic orderings is found when $J_{\text{surface}} \gtrsim 1.6 J_{\text{bulk}}$.

V. SUMMARY

Using element-specific magnetization probes, the temperature evolution of the magnetization in the Gd layers of a strongly coupled Gd/Fe multilayer was studied. Spatially resolved magnetization profiles were obtained from fits of XRMS reflectivity data using dynamic (DWBA) calculation of the asymmetry in the reflected intensity of opposite helicities of incoming circularly polarized x rays. With the fitted parameters, kinematic calculation (BA) was then used to calculate the asymmetry in the reflected intensity. Both approximations include the effect of chemical and magnetic roughness on the scattered intensity, allowing for quantitative determination of magnetization profiles. The refined profiles are inhomogeneous throughout the 20–300 K temperature interval, wherein the magnitude (but not the direction) of the Gd magnetization varies throughout the Gd layer thickness. Different origins for the enhanced Gd magnetic ordering near Fe were discussed, including strong antiferromagnetic coupling at Gd/Fe interfaces, intermixing, and the role of roughness. Theoretical calculations within a mean-field approach show that a strong interlayer antiferromagnetic coupling at Gd/Fe interfaces can account for the observed profiles, even in the absence of chemical roughness. While the enhanced ordering of Gd at Gd/Fe interfaces does not require roughness, these enhanced regions can extend past the very short range of antiferromagnetic interactions in the presence of roughness.

ACKNOWLEDGMENTS

The work at Argonne is supported by the U.S. DOE, Office of Basic Energy Sciences, under Contract No. W-31-109-ENG-38. R.E.C. was supported by the U.S. Army Research Office under Grant No. DAAD19-02-1-0174.

[1] S. S. P. Parkin, Phys. Rev. Lett. **71**, 1641 (1993); P. Beliën, R. Schad, C. D. Potter, G. Verbanck, V. V. Moshchalkov, and Y. Bruynseraede, Phys. Rev. B **50**, 9957 (1994); J. Barnaś and G. Palasantzas, J. Appl. Phys. **82**, 3950 (1997); P. Grünberg, D. E. Bürgler, R. Gareev, D. Olligs, M. Buchmeier, M. Breidbach, B. Kuanr, and R. Schreiber, J. Phys. D **35**, 2403 (2002).

[2] Y. Kamiguchi, Y. Hayakawa, and H. Fujimori, Appl. Phys. Lett. **55**, 1918 (1989); H. Fujimori, Y. Kamiguchi, and Y. Hayakawa, J. Appl. Phys. **67**, 5716 (1990); José L. Prieto, Bas B. van Aken, Gavin Burnell, Chris Bell, Jan E. Evetts, Neil Mathur, and Mark G. Blamire, Phys. Rev. B **69**, 054436 (2004).

[3] J. Nogues and I. K. Schuller, J. Magn. Magn. Mater. **192**, 203 (1999).

[4] M. Grimsditch, A. Hoffmann, P. Vavassori, Hongtao Shi, and D. Lederman, Phys. Rev. Lett. **90**, 257201 (2003).

[5] R. W. Wang, D. L. Mills, Eric E. Fullerton, J. E. Mattson, and S. D. Bader, Phys. Rev. Lett. **72**, 920 (1994).

[6] J. G. LePage and R. E. Camley, Phys. Rev. Lett. **65**, 1152 (1990).

[7] D. Haskel, G. Srajer, Y. Choi, D. R. Lee, J. C. Lang, J. Meerschaut, J. S. Jiang, and S. D. Bader, Phys. Rev. B **67**, 180406(R) (2003).

[8] A. N. Bogdanov and U. K. Rößler, Phys. Rev. Lett. **87**, 037203 (2001).

[9] C. Rau and S. Eichner, Phys. Rev. B **34**, 6347 (1986).

[10] D. Weller, S. F. Alvarado, W. Gudat, K. Schröder, and M. Campagna, Phys. Rev. Lett. **54**, 1555 (1985).

[11] H. Tang, D. Weller, T. G. Walker, J. C. Scott, C. Chappert, H. Hopster, A. W. Pang, D. S. Dessau, and D. P. Pappas, Phys. Rev. Lett. **71**, 444 (1993).

[12] C. Vettier, D. B. McWhan, E. M. Gyorgy, J. Kwo, B. M. Buntschuh, and B. W. Batterman, Phys. Rev. Lett. **56**, 757 (1986).

[13] J. Kwo, E. M. Gyorgy, D. B. McWhan, M. Hong, F. J. DiSalvo, C. Vettier, and J. E. Bower, Phys. Rev. Lett. **55**, 1402 (1985).

[14] M. Taborelli, R. Allenspach, G. Boffa, and M. Landolt, Phys. Rev. Lett. **56**, 2869 (1986).

[15] D. Haskel, G. Srajer, J. C. Lang, J. Pollmann, C. S. Nelson, J. S. Jiang, and S. D. Bader, Phys. Rev. Lett. **87**, 207201 (2001).

[16] N. Ishimatsu, H. Hashizume, S. Hamada, N. Hosoito, C. S. Nelson, C. T. Venkataraman, G. Srajer, and J. C. Lang, Phys. Rev. B **60**, 9596 (1999).

[17] Sang-Kook Kim and J. B. Kortright, Phys. Rev. Lett. **86**, 1347 (2001).

[18] C. S. Nelson, G. Srajer, J. C. Lang, C. T. Venkataraman, S. K. Sinha, H. Hashizume, N. Ishimatsu, and N. Hosoito, Phys. Rev. B **60**, 12 234 (1999).

[19] N. Jaouen, J. M. Tonnerre, D. Raoux, E. Bontempi, L. Ortega, M. Müenzenberg, W. Felsch, A. Rogalev, H. A. Dürr, E. Dudzik, G. van der Laan, H. Maruyama, and M. Suzuki, Phys. Rev. B **66**,

134420 (2002); L. Sève, N. Jaouen, J. M. Tonnerre, D. Raoux, F. Bartolomé, M. Arend, W. Felsch, A. Rogalev, J. Goulon, C. Gautier, and J. F. Bérar, *ibid.* **60**, 9662 (1999).
[20] R. M. Osgood, III, S. K. Sinha, J. W. Freeland, Y. U. Idzerda, and S. D. Bader, J. Appl. Phys. **85**, 4619 (1999).
[21] D. R. Lee, S. K. Sinha, D. Haskel, Y. Choi, J. C. Lang, S. A. Stepanov, and G. Srajer, Phys. Rev. B **68**, 224409 (2003).
[22] J. Geissler, E. Goering, M. Justen, F. Weigand, G. Schütz, J. Langer, D. Schmitz, H. Maletta, and R. Mattheis, Phys. Rev. B **65**, 020405(R) (2001).
[23] J. F. Ankner and G. P. Felcher, J. Magn. Magn. Mater. **200**, 741 (1999).
[24] O. F. K. McGrath, N. Ryzhanova, C. Lacroix, D. Givord, C. Fermon, C. Miramond, G. Saux, S. Young, and A. Vedyayev, Phys. Rev. B **54**, 6088 (1996).
[25] M. Sajieddine, Ph. Bauer, K. Cherifi, C. Dufour, G. Marchal, and R. E. Camley, Phys. Rev. B **49**, 8815 (1994).
[26] G. Schütz, W. Wagner, W. Wilhelm, P. Kienle, R. Zeller, R. Frahm, and G. Materlik, Phys. Rev. Lett. **58**, 737 (1987); J. Stöhr, J. Magn. Magn. Mater. **200**, 470 (1999).
[27] Kenta Amemiya, Soichiro Kitagawa, Daiju Matsumura, Toshihiko Yokoyama, and Toshiaki Ohta, J. Phys.: Condens. Matter **15**, S561 (2003).
[28] K. Namikawa, M. Ando, T. Nakajima, and H. Kawata, J. Phys. Soc. Jpn. **54**, 4099 (1985); D. Gibbs, D. R. Harshman, E. D. Isaacs, D. B. McWhan, D. Mills, and C. Vettier, Phys. Rev. Lett. **61**, 1241 (1988); F. de Bergevin, M. Brunel, R. M. Galéra, C. Vettier, E. Elkaïm, M. Bessière, and S. Lefèbvre, Phys. Rev. B **46**, 10 772 (1992); A. Fasolino, P. Carra, and M. Altarelli, *ibid.* **47**, 3877 (1993); H. A. Dürr, E. Dudzik, S. S. Dhesi, J. B. Goedkoop, G. van der Lan, M. Belakhovsky, C. Mocuta, A. Marty, and Y. Samson, Science **284**, 2166 (1999).
[29] J. P. Hannon, G. T. Trammell, M. Blume, and D. Gibbs, Phys. Rev. Lett. **61**, 1245 (1988).
[30] R. E. Camley and D. R. Tilley, Phys. Rev. B **37**, 3413 (1988).
[31] S. K. Sinha, E. B. Sirota, S. Garoff, and H. B. Stanley, Phys. Rev. B **38**, 2297 (1988).
[32] J. C. Lang and G. Srajer, Rev. Sci. Instrum. **66**, 1540 (1995).
[33] D. T. Cromer and D. Liberman, J. Chem. Phys. **53**, 1891 (1970); J. O. Cross, M. Newville, J. J. Rehr, L. B. Sorensen, C. E. Bouldin, G. Watson, T. Gouder, G. H. Lander, and M. I. Bell, Phys. Rev. B **58**, 11 215 (1998).
[34] Code available upon request (haskel@aps.anl.gov).
[35] J. Miguel-Soriano, J. Chaboy, L. M. García, F. Bartolomé, and H. Maruyama, J. Appl. Phys. **87**, 5884 (2000).
[36] L. G. Parratt, Phys. Rev. **95**, 359 (1954); L. Nevot and P. Croce, Rev. Phys. Appl. **15**, 761 (1980).
[37] C. S. Nelson, Ph.D. thesis, Northwestern University (1999).
[38] M. Blume and D. Gibbs, Phys. Rev. B **37**, 1779 (1988).
[39] S. A. Stepanov and S. K. Sinha, Phys. Rev. B **61**, 15 302 (2000).
[40] J. C. Lang, Xindong Wang, V. P. Antropov, B. N. Harmon, A. I. Goldman, H. Wan, G. C. Hadjipanayis, and K. D. Finkelstein, Phys. Rev. B **49**, 5993 (1994).
[41] J. P. Rueff, R. M. Galéra, S. Pizzini, A. Fontaine, L. M. Garcia, Ch. Giorgetti, E. Dartyge, and F. Baudelet, Phys. Rev. B **55**, 3063 (1997).
[42] V. Holý and T. Baumbach, Phys. Rev. B **49**, 10 668 (1994).
[43] B. T. Thole, Paolo Carra, F. Sette, and G. van der Laan, Phys. Rev. Lett. **68**, 1943 (1992).
[44] Paolo Carra, B. T. Thole, Massimo Altarelli, and Xindong Wang, Phys. Rev. Lett. **70**, 694 (1993).
[45] Xindong Wang, T. C. Leung, B. N. Harmon, and P. Carra, Phys. Rev. B **47**, 9087 (1993).
[46] Hiroshi Matsuyama, Isao Harada, and Akio Kotani, J. Phys. Soc. Jpn. **66**, 337 (1997).
[47] Michel van Veenendaal, J. B. Goedkoop, and B. T. Thole, Phys. Rev. Lett. **78**, 1162 (1997).
[48] Y. Wu, J. Stöhr, B. D. Hermsmeier, M. G. Samant, and D. Weller, Phys. Rev. Lett. **69**, 2307 (1992).
[49] A. Berger, G. Campillo, P. Vivas, J. E. Pearson, S. D. Bader, E. Baca, and P. Prieto, J. Appl. Phys. **91**, 8393 (2002).
[50] K. Binder and P. C. Hohenberg, Phys. Rev. B **9**, 2194 (1974).